POLYMER CHEMISTRY

Chemically circular, mechanically tough, and melt-processable polyhydroxyalkanoates

Li Zhou[1]†, Zhen Zhang[1]†, Changxia Shi[1], Miriam Scoti[1,2], Deepak K. Barange[1], Ravikumar R. Gowda[1], Eugene Y.-X. Chen[1]*

Polyhydroxyalkanoates (PHAs) have attracted increasing interest as sustainable plastics because of their biorenewability and biodegradability in the ambient environment. However, current semicrystalline PHAs face three long-standing challenges to broad commercial implementation and application: lack of melt processability, mechanical brittleness, and unrealized recyclability, the last of which is essential for achieving a circular plastics economy. Here we report a synthetic PHA platform that addresses the origin of thermal instability by eliminating α-hydrogens in the PHA repeat units and thus precluding facile cis-elimination during thermal degradation. This simple α,α-disubstitution in PHAs enhances the thermal stability so substantially that the PHAs become melt-processable. Synergistically, this structural modification also endows the PHAs with the mechanical toughness, intrinsic crystallinity, and closed-loop chemical recyclability.

Polyhydroxyalkanoates (PHAs) are a class of polyester naturally accumulated biologically by living microorganisms (1–8) or synthetically produced chemocatalytically (9, 10) from diverse feedstocks, especially biorenewable sources. They possess tunable thermomechanical properties and are biodegradable in the ambient environment, thus offering a more sustainable alternative to petroleum-derived and/or nondegradable plastics. Over the past 60+ years, the ring-opening polymerization (ROP) of four-membered β-lactones, such as β-butyrolactone (β-BL), and their derivatives with different substituents at α and β positions has been extensively studied to enable the chemical synthesis of PHAs, particularly poly(3-hydroxybutyrate) (P3HB), with atactic, iso-rich, syndio-rich, or syndiotactic stereomicrostructures (tacticities) (9–16). More recently, purely isotactic P3HB that has a number-average molar mass (M_n) of 154 kDa, a narrow dispersity (Đ) of 1.01, and a high melting-transition temperature (T_m) of 171° to 175°C (17); stereo-sequenced PHAs (18); polyolefin-like PHA copolymers (19); and alternating isotactic PHAs (20) have also been realized through the ROP of eight-membered dialkyl diolides (8DL^R). In addition to its isotactic polypropylene (it-PP)–like high T_m, the highly crystalline it-P3HB exhibits excellent barrier properties that are superior to those of commodity plastics widely used in packaging, such as polyethylene (PE) and polyethylene terephthalate (PET) (21). These attractive properties of PHAs, coupled with their biorenewability and biodegradability, offer a promising solution to combat the global plastics problem (22–27).

However, three long-standing challenges facing PHAs must be addressed before broad commercial implementation and applications can be realized. First, current PHAs are intrinsically thermally unstable, with a relatively low degradation temperature (T_d, the temperature at 5% weight loss) of ~250°C, owing to the presence of α-hydrogens that promote facile cis-elimination via the six-membered transition state to form an internal alkene and a carboxylic acid (Fig. 1A) (28–31), causing a large, continuous drop in shear viscosity under melt-processing conditions (Fig. 1B). Second, the mechanical performance of PHAs is generally inferior to that of commonly used plastics; for example, it-P3HB is extremely brittle with an elongation at break (ε_b) ~4%, which is much lower than that of it-PP (ε_b > 400%). Third, synthetic PHAs lack the desired closed-loop chemical recyclability. For example, the acid-catalyzed depolymerization of P3HB leads to formation of cyclic oligomers (which can be repolymerized to only oligomers with M_n ~5 kDa) (32, 33), rather than its readily polymerizable monomer β-BL or 8DL^{Me} to close the loop, whereas the base-catalyzed depolymerization yields crotonic acid (34). Although biodegradability in the ambient environment is a distinct advantage of PHAs for protecting our environment if they are disposed there, they should not be landfilled as accumulation of degraded intermediates and eventual CO_2 will cause unintended environmental and climate problems. Additionally, the inability to recover the PHA building blocks represents a considerable loss of energy and resources that are still endowed in the postconsumer PHAs. Hence, it is critical to install the chemical circularity to the biodegradable PHAs toward an ultimate goal of establishing a circular plastics economy (35, 36).

Strategies to suppress thermal degradation and achieve melt processability

A straightforward strategy to suppress thermal degradation due to cis-elimination enabled by α-hydrogens in conventional PHAs is to substitute both α-hydrogens with alkyl or aryl groups. When substituting only one α-hydrogen in the parent P3HB with a methyl group, the resulting poly(3-hydroxy-2-methylbutyrate) indeed shows improved thermal stability, but only by ~20°C relative to the P3HB used in that study (37). However, substituting both α-hydrogens yields poly(3-hydroxy-2,2-dimethylbutyrate) [P3H(Me)$_2$B], the thermal and mechanical properties of which are drastically enhanced: P3H(Me)$_2$B is not only semicrystalline, with high T_m's of 167° to 243°C as well as being thermally stable with high T_d's of 314° to 335°C (i.e., 56° to 85°C enhancement) and melt-processable, but also ductile, with ε_b >200% (Fig. 1, C and D). Moreover, P3H(Me)$_2$B can be chemically recycled back to its starting monomer, α,α-dimethyl-β-butyrolactone [(Me)$_2$BL], which is used in the chain-growth ROP, or 3-hydroxy-2,2-dimethylbutyric acid [3H(Me)$_2$BA], which is used in the step-growth polycondensation (SGP), thus accomplishing closed-loop chemical recyclability (Fig. 1C). Poly(3-hydroxy-2,2-dimethylpropionate), P3H(Me)$_2$P (M_n = 162 kDa, prepared from the ROP of α,α-dimethyl-β-propiolactone, table S1) also exhibits high T_d (up to 373°C) and T_m (up to 232°C) values, but it is extremely brittle with ε_b < 4% (figs. S1 to S3). The ROP of (Me)$_2$BL (prepared from highly reactive dimethyl ketene and acetaldehyde) was attempted, but only oligomeric species (M_n = 2.9 kDa) were obtained in 35% yield after 10 days (38). The method reported herein enabled the rapid synthesis of high–molar mass P3H(Me)$_2$B in quantitative yield and with M_n up to 554 kDa, T_m up to 243°C, and T_d up to 335°C. Overall, such thermal robustness of α,α-dimethylated PHAs enables their melt processability, despite further enhanced T_m values, and such PHAs exhibit the desired chemical circularity through closing the monomer-polymer-monomer loop.

## Dual closed loops to achieve chemical circularity

The α,α-dimethylated PHA can be synthesized through either the SGP of hydroxyacid (HA) 3H(Me)$_2$BA or the ROP of lactone (Me)$_2$BL (Fig. 1C). The HA, 3H(Me)$_2$BA, was obtained in one step from acetaldehyde, which is produced at a large industrial scale and can also be biosourced, and isobutyric acid, a commercial chemical that can be obtained biologically from glucose (39), in 88% yield (see materials and methods for its synthesis at 362-g scale from methyl isobutyrate), whereas the lactone (Me)$_2$BL was prepared via one-step lactonization of the HA [e.g., 232 g of (Me)$_2$BL was

[1]Department of Chemistry, Colorado State University, Fort Collins, CO 80523-1872, USA. [2]Dipartimento di Scienze Chimiche, Università di Napoli Federico II, Complesso Monte S. Angelo, Via Cintia, 80126 Napoli, Italy.
*Corresponding author: Email: eugene.chen@colostate.edu
†These authors contributed equally to this work.
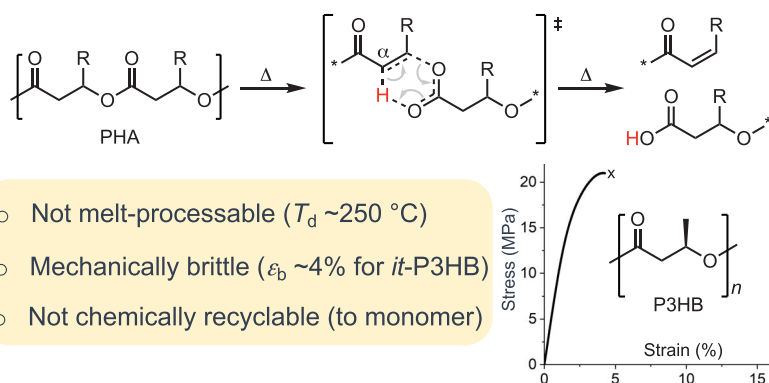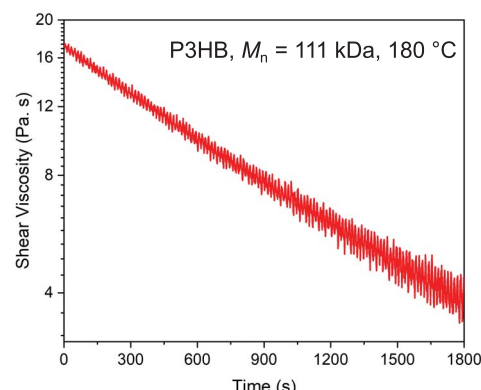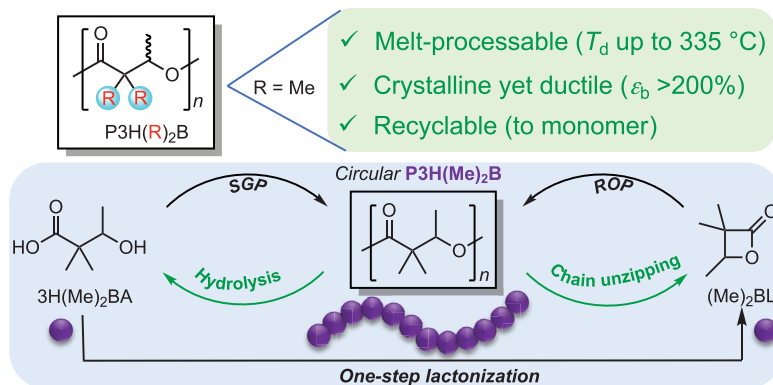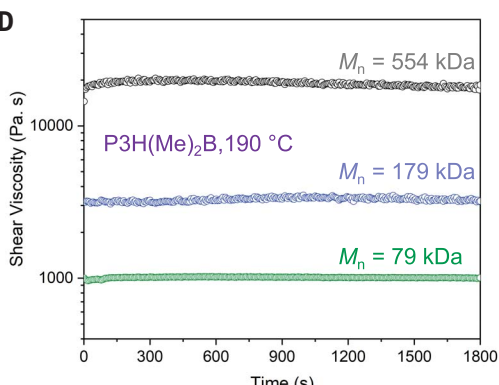
Fig. 1. Progress in PHA design. (**A**) Three challenges facing the current PHA (P3HB, in particular). (**B**) Shear viscosity (shear rate $\dot{r} = 1\ s^{-1}$) in melt (180°C) of *it*-P3HB (M_n = 111 kDa), showing a large, continuous drop in viscosity over 30 min owing to rapid degradation. Data were acquired from this study. (**C**) Redesigned α,α-disubstituted PHAs, P3H(R)$_2$B, devoid of α-hydrogens synergistically combine three desirable properties. Chemical circularity was achieved through closing both the hydroxyacid SGP, base-catalyzed hydrolysis and lactone ROP, based-catalyzed chain-unzipping loops for P3H(Me)$_2$B. (**D**) Shear viscosity ($\dot{r}$ = 1 s^{-1}) in melt (190°C) of P3H(Me)$_2$B with medium to high molar mass (M_n = 79 – 554 kDa), showing no decrease in viscosity over 30 min, indicating melt processability.

prepared in 93% yield]. The diethyl derivative, (Et)$_2$BL, was synthesized by use of the same lactonization method. Notably, the HA and lactone monomers can be prepared or recovered in good to quantitative yields from selective depolymerization of the PHA (see below).

At the outset, the ROP of (Me)$_2$BL (as a racemate) was explored by using different organic base catalysts and reaction conditions, and the ROP was optimized with superbase catalyst ^{t}Bu-P$_4$ {1-*tert*-butyl-4,4,4-tris(dimethyl-amino)-2,2-bis[tris(dimethylamino)phosphoranyliden-amino]2λ^5,4λ^5-catenadi(phosphazene)} in tetrahydrofuran (THF) at 70°C (table S1). Thus, the ROP in THF, with ^{t}Bu-P$_4$ as the catalyst and benzyl alcohol (BnOH) as the initiator, afforded P3H(Me)$_2$B with low M_n (22.1 kDa, Đ = 1.02) to medium M_n (43.0 kDa, Đ = 1.05) to high M_n (179 kDa, Đ = 1.04; 554 kDa, Đ = 1.06). Likewise, the ROP of (Et)$_2$BL in THF also led to the corresponding high–molar mass P3H(Et)$_2$B (M_n = 468 kDa, Đ = 1.18) in near-quantitative yield (table S1). In a separate set of experiments that investigated the degree

of control in the ROP, the molar mass was found to increase linearly with an increase of the [(Me)$_2$BL]/[^{t}Bu-P$_4$] ratio from 200:1 to 1600:1, whereas the dispersity of the resulting P3H(Me)$_2$B remained extremely narrow (Đ ≤ 1.04), indicating the well-controlled ROP of (Me)$_2$BL (Fig. 2, A and B). The scalability of this ROP was tested in a polymerization using 125 g of (Me)$_2$BL under industrially relevant conditions: with a low catalyst loading [55 parts per million (ppm) ^{t}Bu-P$_4$], neat (solvent-free), and at 70°C. This scaled-up run achieved 96% monomer conversion and afforded 115 g of the pure P3H(Me)$_2$B in a 92% isolated yield.

To prepare a purely isotactic polymer sample for stereomicrostructural and thermal property analysis, we synthesized (S)-P3H(Me)$_2$B (M_n = 34.9 kDa, Đ = 1.15) via the ROP of enantiopure (S)-(Me)$_2$BL. The perfect tacticity was characterized by the presence of only one carbonyl signal at 176.4 ppm and also a single signal at 46.9 and 12.6 ppm in ^{13}C nuclear magnetic resonance (NMR) spectra for the quaternary and methyl carbons, respectively

(Fig. 2C). In comparison, the P3H(Me)$_2$B derived from (Me)$_2$BL with a 70:30 (S)/(R) ratio showed multiple signals in those regions, but most informatively, the new minor signal appeared at 45.91 ppm next to the 45.87-ppm major signal, indicative of an iso-rich tacticity. As predicted, those two signals present in the P3H(Me)$_2$B that was prepared from a 50:50 (S)/(R) ratio are approximately in equal abundance (Fig. 2C), indicating an atactic structure.

We envisioned another synergistic benefit of α,α-disubstitution that could endow the α,α-dialkylated PHA with chemical recyclability by direct depolymerization to its monomer, enabled by the *gem*-disubstituted Thorpe–Ingold effect that promotes ring closure and stabilization of strained rings (*40–44*). At the outset, depolymerization of a ROP-derived P3H(Me)$_2$B sample was screened at temperatures below 240°C under vacuum with different base catalysts (table S2), affording (Me)$_2$BL and side-product 2-methyl-2-butene with different ratios (fig. S18). For example, heating the sample with NaOH (5 wt %) at 210°C under
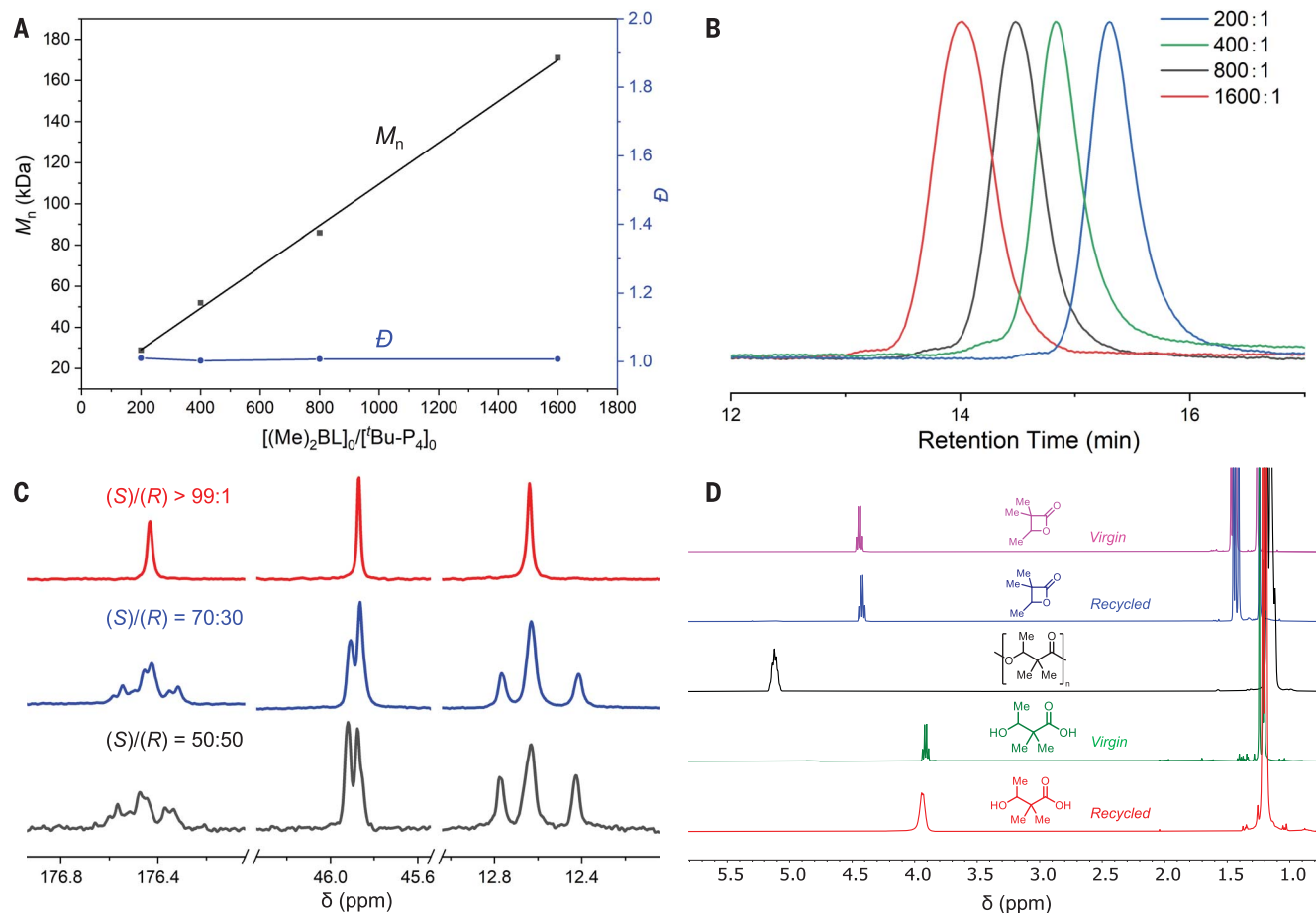
Fig. 2. ROP characteristics and chemical circularity. (**A**) Plots of M_n and Đ values of the resulting P3H(Me)$_2$B as a function of the [(Me)$_2$BL]/[^{t}Bu-P$_4$] ratio (Me)$_2$BL/^{t}Bu-P$_4$ = 200:1, 400:1, 800:1, 1600:1; M_n (Đ) = 28.9 kDa (1.01), 51.9 kDa (1.01), 85.9 kDa (1.01), 179 kDa (1.04). (**B**) Size exclusion chromatography (SEC) curves for the P3H(Me)$_2$B samples produced at the different [(Me)$_2$BL]/[^{t}Bu-P$_4$] ratios. (**C**) Overlays of ^{13}C NMR spectra [(CF$_3$)$_2$CDOD] of P3H(Me)$_2$B derived from (Me)$_2$BL/^{t}Bu-P$_4$/BnOH = 800:0.5:1: (S)-(Me)$_2$BL/(R)-(Me)$_2$BL > 99:1 (red), = 70:30 (blue), = 50:50 (black). (**D**) Overlays of ^{1}H NMR spectra (23°C, CDCl$_3$) of the virgin (pink) and recycled (blue) lactone (Me)$_2$BL, virgin P3H(Me)$_2$B (black), and virgin (green) and recycled (red) HA monomer 3H(Me)$_2$BA.

vacuum recovered the pure (Me)$_2$BL monomer in 60% isolated yield (Fig. 2D and fig. S19) after the quick release of 2-methyl-2-butene as a gas, which was also recovered and could be reused. Next, through consecutive polymerization-depolymerization cycles, we achieved the circular monomer-polymer-monomer loop.

The second pathway to establish the closed-loop chemical recycling is through hydrolytic depolymerization of the PHA to the HA. For example, hydrolysis of P3H(Me)$_2$B (table S3) by aqueous LiOH enabled its depolymerization to form pure 3H(Me)$_2$BA in quantitative yield (Fig. 2D and fig. S21). The recovered HA can be transformed to (Me)$_2$BL via one-step lactonization (Fig. 1C). (Me)$_2$BL can also be obtained through NaOH (2 wt %)–catalyzed depolymerization of the oligomeric P3H(Me)$_2$B prepared through the SGP of 3H(Me)$_2$BA catalyzed by BF$_3$·OEt$_2$ (Fig. 1C and fig. S22). These results demonstrate that the SGP of the HA can be used to obtain oligo-

mers or polymers with low to medium molar mass, which are effectively depolymerized to form the lactone for the rapid ROP to high–molar mass PHAs.

Thermal properties and tacticity-independent (intrinsic) crystallinity

The isotactic (R)-P3H(Me)$_2$B exhibits a notably high T_m of 243°C (Fig. 3A and fig. S24), which is 68°C higher than that of (R)-P3HB (T_m = 175°C) (17). Moreover, the atactic at-P3H(Me)$_2$B, which is produced by the ROP of rac-(Me)$_2$BL catalyzed by the achiral organic catalyst ^{t}Bu-P$_4$, is also semicrystalline, with T_m values of 167° and 176°C (Fig. 3A and fig. S25). Thus, P3H(Me)$_2$B adds to rare examples of polymers exhibiting tacticity-independent crystallinity—a class of polymers that are intrinsically semicrystalline, having a similar degree of crystallinity regardless of the backbone tacticity, although the absolute T_m value varies as the tacticity changes (45, 46). To probe the possibility of

stereocomplex formation, we prepared a 1:1 physical blend of enantiomeric it-polymers derived from enantiomeric monomers, (R)-(Me)$_2$BL and (S)-(Me)$_2$BL, and found the resulting blend to display the same thermal properties as the homochiral polymers, suggesting the absence of stereocomplexation (fig. S27). Furthermore, the iso-rich P3H(Me)$_2$B derived from (Me)$_2$BL with a 70/30 (S)/(R) ratio showed T_m values of 189° and 204°C, which are between those of the it- and at-P3H(Me)$_2$B samples (Fig. 3A and fig. S28).

The two melting peaks observed in all the melt-crystallized P3H(Me)$_2$B samples present in the second heating scan (but not in the first heating scan) on the differential scanning calorimetry (DSC) thermograms, which become more pronounced as the tacticity decreases (Fig. 3A), could be due to the melting of two different polymorphic forms crystallized by cooling from the melt; to a transformation between two different crystalline forms; or
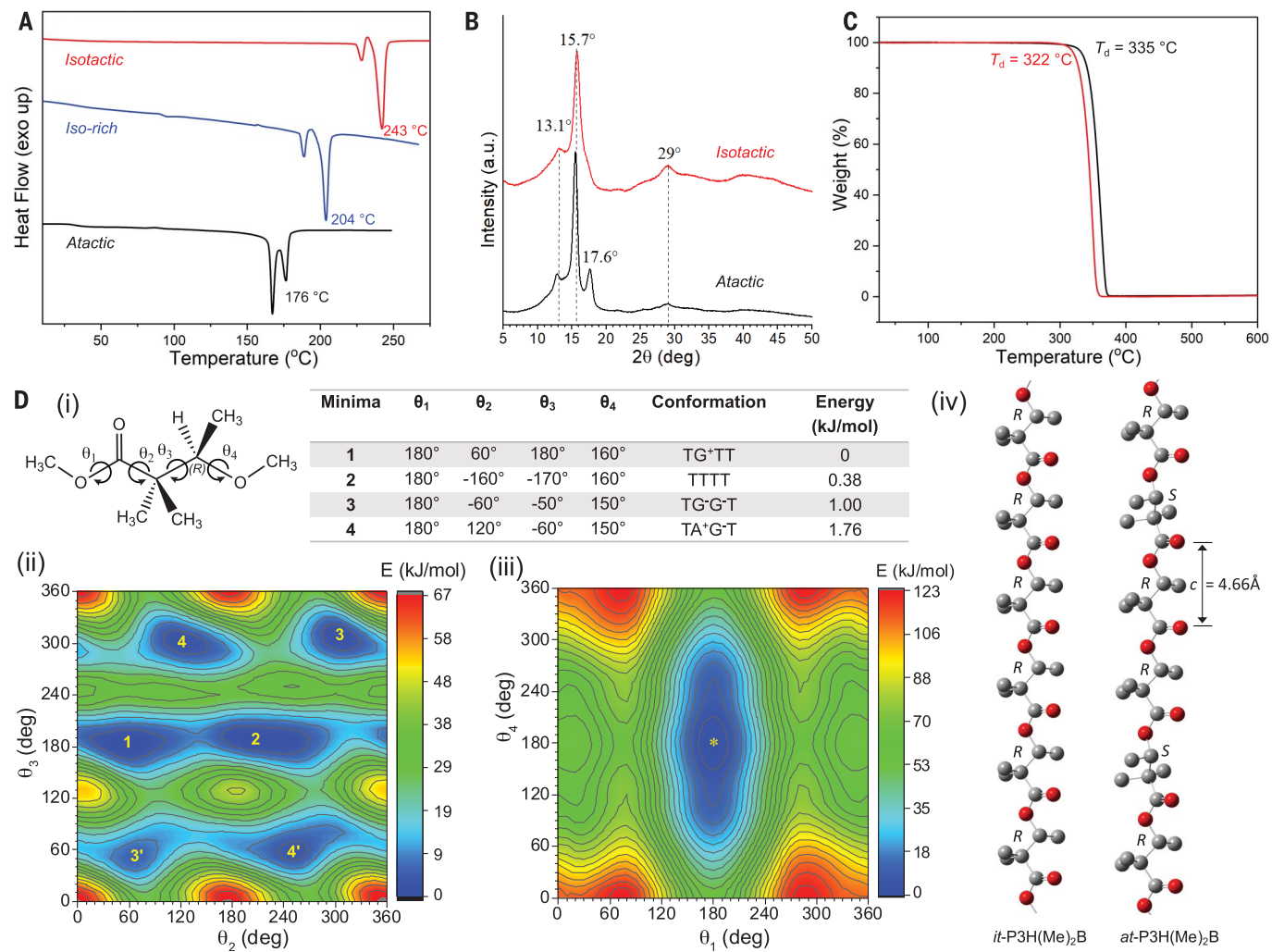
Fig. 3. Intrinsic crystallinity and high thermal stability. (**A**) Second heating DSC scan (10°C/min) curves for isotactic (red), iso-rich (blue), and atactic (black) P3H(Me)$_2$B materials. (**B**) WAXS profiles of it-P3H(Me)$_2$B (red) and at-P3H(Me)$_2$B (black), showing nearly identical diffraction patterns and a similar degree of crystallinity. (**C**) TGA curves for it-P3H(Me)$_2$B (red) and at-P3H (Me)$_2$B (black), showing a 13°C higher T_d for at-P3H(Me)$_2$B. (**D**) (i) Definition of the fragment of the chain of it-(R)-P3H(Me)$_2$B and torsion angles θ_1, θ_2, θ_3, and θ_4, with their values corresponding to the four conformational models and relative energy. (ii) Conformational energy map as a function of the torsion angles θ_2 and θ_3 scanned every 10° with θ_1 and θ_4 fixed at 180°. The energy levels are reported every 5 kJ/mol, and the energy minima are indicated with numbers. The scale of the values of energy is indicated on the right with different colors, with the energy increasing from blue (the energy minima) to red. The energy values are scaled with respect to the absolute minimum at E = 0 kJ/mol. The minima corresponding to a number and its prime number (**3** and **3'**, **4** and **4'**) are symmetrically equivalent. (iii) Conformational energy map as a function of θ_1 and θ_4 scanned every 10° with θ_2 and θ_3 fixed at θ_2 = −160° and θ_3 = −170° (minimum **2**). The energy levels are reported every 5 kJ/mol, and the value of the absolute energy minimum is indicated with an asterisk. (iv) Low-energy models of the transplanar conformation (TTTT) for the chains of it-(R)-P3H(Me)$_2$B and at-P3H(Me)$_2$B viewed along the chain axis.

simply to melting and recrystallization into the same crystalline form. To clarify this point, three DSC experiments with second heating scans performed at different heating rates (2.5, 10, and 20°C/min) were carried out. The decrease in the area of the higher T_m peak and the simultaneous increase in the area of the lower T_m peak with increasing the heating rate (figs. S32 and S33) suggest that the two peaks are not due to the melting of two different crystalline phases formed upon cooling from the melt, but rather indicate that melting

and recrystallization phenomena occur during heating. To further test this hypothesis, we also collected wide-angle x-ray scattering (WAXS) profiles at different temperatures during heating of the melt-crystallized sample (fig. S34), showing the identical profiles between those collected at room temperature before the first heating scan and after the crystallization from the melt. These results confirm the absence of two different polymorphic forms and suggest that the two melting peaks are due to melting at nearly 167° to 169°

C and fast recrystallization of the melt with formation of more-ordered and thick crystals of the same crystalline form that melt at higher temperatures of 177° to 181°C. The result that the temperatures of both melting peaks increase with decreasing heating rate is a further confirmation of the occurrence of recrystallization during heating.

The WAXS profile of the as-synthesized at-P3H(Me)$_2$B (M_n = 554 kDa) displays three major diffraction peaks centered at $2\theta \approx$ 13.1°, 15.7°, and 17.6°, and other minor diffraction
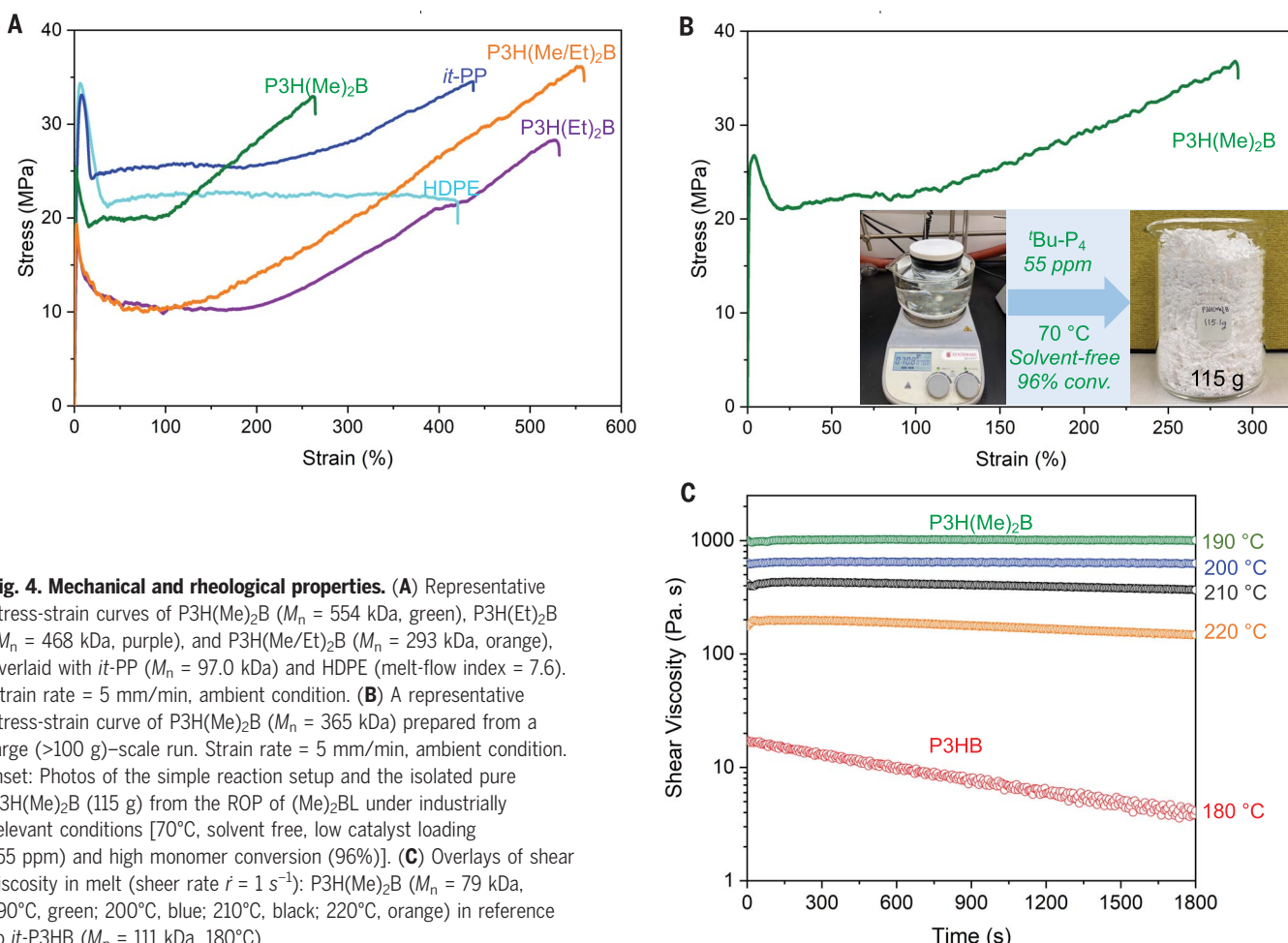
Fig. 4. Mechanical and rheological properties. (**A**) Representative stress-strain curves of P3H(Me)$_2$B (M_n = 554 kDa, green), P3H(Et)$_2$B (M_n = 468 kDa, purple), and P3H(Me/Et)$_2$B (M_n = 293 kDa, orange), overlaid with *it*-PP (M_n = 97.0 kDa) and HDPE (melt-flow index = 7.6). Strain rate = 5 mm/min, ambient condition. (**B**) A representative stress-strain curve of P3H(Me)$_2$B (M_n = 365 kDa) prepared from a large (>100 g)–scale run. Strain rate = 5 mm/min, ambient condition. Inset: Photos of the simple reaction setup and the isolated pure P3H(Me)$_2$B (115 g) from the ROP of (Me)$_2$BL under industrially relevant conditions [70°C, solvent free, low catalyst loading (55 ppm) and high monomer conversion (96%)]. (**C**) Overlays of shear viscosity in melt (sheer rate $\dot{r}$ = 1 s^{-1}): P3H(Me)$_2$B (M_n = 79 kDa, 190°C, green; 200°C, blue; 210°C, black; 220°C, orange) in reference to *it*-P3HB (M_n = 111 kDa, 180°C).

peaks of much lower intensities at higher 2θ values (Fig. 3B), with the calculated crystallinity (x_c) of 67% (fig. S35). When the as-synthesized *it*- and *at*-P3H(Me)$_2$B materials are compared, they display essentially the same main diffraction peaks with slightly different intensities at the higher 2θ region (Fig. 3B); indeed, the degree of crystallinity of *at*-P3H(Me)$_2$B (x_c = 67%) was found to be even higher than that of *it*-P3H(Me)$_2$B (x_c = 58%, fig. S36). To understand the origin of crystallinity manifested in *at*-P3H(Me)$_2$B, we performed conformational analysis, first on chain models of *it*-P3H(Me)$_2$B [Fig. 3D, (i) to (iii)] with opposite chirality—namely, (*R*)-P3H(Me)$_2$B and (*S*)-P3H(Me)$_2$B—and then extended to a chain model of *at*-P3H(Me)$_2$B characterized by a random succession of *R* and *S* units along the chain (supplementary text and figs. S37 to S42). Oriented fibers of *at*-P3H(Me)2B were obtained by stretching the compression-molded sample at ~150°C and annealing the fiber under tension at 143°C for 35 min. The two-dimensional x-ray fiber diffraction pattern of *at*-P3H(Me)2B (fig. S40) reveals three strongest reflections that are polarized on the equator and centered at the same 2θ position as those observed in the

powder profile (Fig. 3B). These results indicate that the fiber is crystallized in the same crystalline form of the as-prepared and melt-crystallized samples and that upon stretching, no polymorphic transformations occur. Other reflections are polarized on the first layer line and further weak reflections on the second layer line. From the separation between the different layer lines observed in the fiber pattern, a value of the chain axis *c* of 4.66 Å was determined. This value is consistent with a transplanar conformation corresponding to one of the energy minima found by the conformational analysis [Fig. 3D, (i) to (iii), and figs. S37 to S42]. Overall, this study showed that the shape of the chain and the projection normal to the chain axis of *at*-P3H(Me)$_2$B are very similar to the ordered models of the *R*-enantiomer [Fig. 3D, (iv), and figs. S40 to S42], which explains the fact that the *at*-P3H(Me)$_2$B chains can crystallize, despite the configurational disorder, and that the *at*-P3H(Me)$_2$B shows a WAXS profile similar to that of the pure enantiomeric (*R*)-P3H(Me)$_2$B. Indeed, they likely crystallize in the same crystalline form (Fig. 3B).

The thermal stability of the PHA samples was analyzed and compared by thermogravimetric analysis (TGA). Despite the largely different T_m values between *it*- and *at*-P3H(Me)$_2$B materials, they displayed similarly high T_d values of 322° and 335°C, respectively (Fig. 3C and figs. S44 and S45). These values are considerably higher than the T_d value (~250°C) of *it*-P3HB (*17*). The molar mass has a substantial effect on T_d, but it hardly affects T_m. For example, the T_d of P3H(Me)$_2$B increased from 314° to 335°C as the M_n increased from 179 to 554 kDa, whereas the T_m remained the same.

Mechanical and rheological properties

When compared to *it*-P3HB (ε_b ~4%), semi-crystalline *at*-P3H(Me)$_2$B (M_n = 554 kDa) displays a significantly enhanced ductility (ε_b = 228 ± 24.6%), a higher elastic modulus (E = 2.94 ± 0.40 GPa), and a higher stress (σ = 31.6 ± 1.8 MPa), showing that the α,α-dimethyl substitution also overcomes the brittleness of *it*-P3HB (Fig. 4A, table S4, and fig. S56). With incorporation of more flexible diethyl groups, P3H(Et)$_2$B achieved further enhanced ductility with ε_b = 501 ± 36%, while maintaining a high modulus of E = 1.22 ± 0.27 GPa (Fig. 4A, table S5, and fig. S57). The Me/Et random copolymer

P3H(Me/Et)$_2$B, synthesized by copolymerizing (Me)$_2$BL and (Et)$_2$BL (figs. S17 and S58), exhibited an even higher fracture strain (ε_b = 517 ± 35%) and stress (σ = 34.1 ± 2.1 MPa) relative to P3H(Et)$_2$B, which outperformed both high-density PE (HDPE) and it-PP (Fig. 4A, table S6, and fig. S59). Also, the mechanical performance of the P3H(Me)$_2$B material (M_n = 332 kDa) prepared from a large (115 g)–scale run was further improved relative to the polymer prepared at 5-g scale, exhibiting higher elastic modulus (E = 3.08 ± 0.18 GPa), stress (σ = 33.9 ± 2.1 MPa), and ductility (ε_b = 252 ± 30.1%) (Fig. 4B, table S7, and fig. S60). These results further indicate the scalability of the polymerization to produce high-performance P3H(Me)$_2$B.

The third synergy as a result of removing the two cis-elimination–prone α-protons by α,α-dialkyl substitution to enhance the PHA thermal stability in the solid state is the realization of melt processability. To test the possibility of melt processing, we monitored the shear viscosity change over time for P3H(Me)$_2$B at temperatures above T_m in a continuous-flow mode at a shear rate of 1 s^{-1}. As a reference, it-P3HB (M_n = 111 kDa, T_m = 170°C) was also subjected to the same shear viscosity test in melt (180°C). The shear viscosity for P3H(Me)$_2$B (M_n = 79 kDa) remained constant without any obvious decrease over a time frame of 30 min at temperatures up to 210°C (Fig. 4C), which is well above the corresponding melting temperature. Furthermore, P3H(Me)$_2$B samples with a wide molar mass range, from M_n = 79 to 554 kDa, behaved similarly and showed a stable shear viscosity at 190°C over the same time period (Fig. 1D), further demonstrating melt-processing feasibility. By contrast, it-P3HB, known for rapid degradation in melt, displayed a substantial decay in its shear viscosity, from 17 to 4 Pa·s (76%), after 30 min at 180°C (Fig. 4C). P3H(Me)$_2$B (M_n = 79 kDa) evidenced a small but noticeable decrease in its shear viscosity at 220°C, indicating its upper-limit melt-processing temperature (Fig. 4C). Overall, the studies in shear viscosity presented here consolidate the effectiveness of the strategy of removing the α-protons of the PHA repeat units to enhance their thermal stability and enable their melt processability.

A large body of studies have focused on fine-tuning the PHA thermal and mechanical properties by varying the main-chain compositions and stereomicrostructures, as well as the β-pendent group chain length and functionality, achieving notable success in addressing some aspects of the PHA's long-standing challenges but leaving inherent issues with thermal stability and chemical circularity unresolved. The α,α-dialkylated PHA platform described in this study is designed to address the root cause of the PHA thermal instability—

the facile cis-elimination process during thermal degradation involving the α-hydrogens in the repeat units—by substituting both α-hydrogens with alkyl groups. This simple α,α-dialkyl substitution not only enhances the thermal stability so substantially that the PHAs become melt processable but also synergistically endows the PHAs with the high ductility and toughness that are comparable with or superior to it-PP and HDPE. Furthermore, this platform offers ease of synthesis as, in contrast to the parent P3HB, the α,α-dimethylated P3H(Me)$_2$B is always semicrystalline, regardless of its tacticity, thanks to its fascinating tacticity-independent, intrinsic crystallinity, thereby allowing for the synthesis of semicrystalline high-performance PHAs without the need to control the polymerization stereochemistry that often requires specifically designed chiral catalysts. Above all, this design achieves chemical circularity through closing both the ROP and SGP loops in PHA production and chemical recycling to monomer, thereby solving the three challenges facing the current PHAs.

REFERENCES AND NOTES

1. D. K. Bedade, C. B. Edson, R. A. Gross, *Molecules* **26**, 3463 (2021).
2. D. Tan, Y. Wang, Y. Tong, G.-Q. Chen, *Trends Biotechnol.* **39**, 953–963 (2021).
3. A. Anjum et al., *Int. J. Biol. Macromol.* **89**, 161–174 (2016).
4. S. Muhammadi, Shabina, M.Afzal, S.Hameed, *Green Chem. Lett. Rev.* **8**, 56–77 (2015).
5. B. Laycock, P. Halley, S. Pratt, A. Werker, P. Lant, *Prog. Polym. Sci.* **38**, 536–583 (2013).
6. S. Taguchi, T. Iwata, H. Abe, Y. Doi, in *Polymer Science: A Comprehensive Reference*, K. Matyjaszewski, M. Möller., Eds. (Elsevier B.V., 2012), vol. 9, pp. 157–182 .
7. R. W. Lenz, R. H. Marchessault, *Biomacromolecules* **6**, 1–8 (2005).
8. K. Sudesh, H. Abe, Y. Doi, *Prog. Polym. Sci.* **25**, 1503–1555 (2000).
9. H. Li, R. M. Shakaroun, S. M. Guillaume, J. F. Carpentier, *Chem. Eur. J.* **26**, 128–138 (2020).
10. A. H. Westlie, E. C. Quinn, C. R. Parker, E. Y.-X. Chen, *Prog. Polym. Sci.* **134**, 101608 (2022).
11. A. Amgoune, C. M. Thomas, S. Ilinca, T. Roisnel, J. F. Carpentier, *Angew. Chem. Int. Ed.* **45**, 2782–2784 (2006).
12. E. W. Dunn, G. W. Coates, *J. Am. Chem. Soc.* **132**, 11412–11413 (2010).
13. T. Ebrahimi, D. C. Aluthge, S. G. Hatzikiriakos, P. Mehrkhodavandi, *Macromolecules* **49**, 8812–8824 (2016).
14. L. R. Rieth, D. R. Moore, E. B. Lobkovsky, G. W. Coates, *J. Am. Chem. Soc.* **124**, 15239–15248 (2002).
15. J. C. Yang, J. Yang, W. B. Li, X. B. Lu, Y. Liu, *Angew. Chem. Int. Ed.* **61**, e202116208 (2022).
16. M. Zintl et al., *Angew. Chem. Int. Ed.* **47**, 3458–3460 (2008).
17. X. Tang, E. Y.-X. Chen, *Nat. Commun.* **9**, 2345 (2018).
18. X. Tang, A. H. Westlie, E. M. Watson, E. Y.-X. Chen, *Science* **366**, 754–758 (2019).
19. X. Tang et al., *Angew. Chem. Int. Ed.* **132**, 7955–7964 (2020).
20. Z. Zhang, C. Shi, M. Scoti, X. Tang, E. Y.-X. Chen, *J. Am. Chem. Soc.* **144**, 20016–20024 (2022).
21. A. Sangroni et al., *Nat. Commun.* **10**, 3559 (2019).
22. C. Jehanno et al., *Nature* **603**, 803–814 (2022).
23. L. D. Ellis et al., *Nat. Catal.* **4**, 539–556 (2021).
24. B. A. Abel, R. L. Snyder, G. W. Coates, *Science* **373**, 783–789 (2021).
25. J.-B. Zhu, E. M. Watson, J. Tang, E. Y.-X. Chen, *Science* **360**, 398–403 (2018).
26. K. P. Sullivan et al., *Science* **378**, 207–211 (2022).
27. M. Häußler, M. Eck, D. Rothauer, S. Mecking, *Nature* **590**, 423–427 (2021).
28. Y. Aoyagi, K. Yamashita, Y. Doi, *Polym. Degrad. Stabil.* **76**, 53–59 (2002).
29. N. Grassie, E. Murray, P. Holmes, *Polym. Degrad. Stabil.* **6**, 127–134 (1984).
30. H. Morikawa, R. H. Marchessault, *Can. J. Chem.* **59**, 2306–2313 (1981).
31. C. DePuy, R. King, *Chem. Rev.* **60**, 431–457 (1960).
32. D. Seebach, H. M. Müller, H. M. Bürger, D. A. Plattner, *Angew. Chem. Int. Ed.* **31**, 434–435 (1992).
33. M. Melchiors, H. Keul, H. Höcker, *Macromolecules* **29**, 6442–6451 (1996).
34. H. Ariffin, H. Nishida, Y. Shirai, M. A. Hassan, *Polym. Degrad. Stab.* **95**, 1375–1381 (2010).
35. M. Hong, E. Y.-X. Chen, *Green Chem.* **19**, 3692–3706 (2017).
36. G. W. Coates, Y. D. Getzler, *Nat. Rev. Mater.* **5**, 501–516 (2020).
37. S. Furutate et al., *NPG Asia Mater.* **13**, 31 (2021).
38. M. Brestaz, N. Desilles, G. Le, C. Bunel, *J. Polym. Sci. A Polym. Chem.* **49**, 4129–4138 (2011).
39. K. Lang, J. Zierow, K. Buehler, A. Schmid, *Microb. Cell Fact.* **13**, 2 (2014).
40. S. M. Bachrach, *J. Org. Chem.* **73**, 2466–2468 (2008).
41. M. E. Jung, G. Piizzi, *Chem. Rev.* **105**, 1735–1766 (2005).
42. W. Xiong et al., *Chem* **6**, 1831–1843 (2020).
43. X.-L. Li, R. W. Clarke, J.-Y. Jiang, T.-Q. Xu, E. Y.-X. Chen, *Nat. Chem.* **15**, 278–285 (2023).
44. J. Zhou, D. Sathe, J. Wang, *J. Am. Chem. Soc.* **144**, 928–934 (2022).
45. L.-B. W. Lee, R. A. Register, *Macromolecules* **38**, 1216–1222 (2005).
46. C. Shi et al., *Sci. Adv.* **6**, eabc0495 (2020).

SUPPLEMENTARY MATERIALS

science.org/doi/10.1126/science.adg4520
Materials and Methods
Supplementary Text
Figs. S1 to S60
Tables S1 to S7
References (47–57)